

**Characteristic boundary conditions for simulations of compressible reacting  
flows with multi-dimensional, viscous, and reaction effects**

Chun Sang Yoo and Hong G. Im<sup>\*</sup>

Department of Mechanical Engineering, University of Michigan, Ann Arbor, MI 48109-2125

\* Corresponding author:

Hong G. Im  
Department of Mechanical Engineering  
University of Michigan  
2250 G.G. Brown Bldg.  
2350 Hayward St.  
Ann Arbor, MI 48109-2125.

Phone : (734) 615-5152 (Office)  
Fax : (734) 647-3170  
Email : [hgim@umich.edu](mailto:hgim@umich.edu)

Submitted to Combustion Theory and Modelling

Revised May 2, 2006

**Final Version June 29, 2006**

## **Abstract**

A generalized formulation for the characteristic boundary conditions for compressible reacting flows is proposed. The new and improved approach resolves a number of lingering issues of spurious solution behavior encountered in turbulent reacting flow simulations in the past. This is accomplished (a) by accounting for all the relevant terms in the determination of the characteristic wave amplitudes and (b) by accommodating a relaxation treatment for the transverse gradient terms with the relaxation coefficient properly determined by the low Mach number asymptotic expansion. The new boundary conditions are applied to a comprehensive set of test problems, including vortex-convection, turbulent inflow, ignition front propagation, non-reacting and reacting Poiseuille flows, and counterflow cases. It is demonstrated that the improved boundary conditions perform consistently superior to existing approaches, and result in robust and accurate solutions with minimal acoustic wave interactions at the boundary in hostile turbulent combustion simulation conditions.

**Keywords:** characteristic boundary conditions; compressible reacting flows; direct numerical simulation; locally one-dimensional inviscid approximation; low Mach number asymptotics.

## 1. Introduction

One of the common issues in the simulation of compressible Navier-Stokes equations is the treatment of physical boundary conditions. In many high-fidelity simulations, the computational domain size is often limited due to cost consideration, so that it is inevitable to impose domain boundaries where a significant flow action is present. These artificial boundaries can result in spurious reflections of physical information, thereby adversely affecting the accuracy and stability of the solutions. Therefore, careful removal of unwanted boundary effects has been a research subject for many years.

Previous studies on the characteristic boundary conditions have focused on how to suppress acoustic wave reflections at open boundaries. A general form of nonreflecting outflow boundary conditions was derived based on the system of hyperbolic equations [1, 2], where several approximations were introduced in order to ensure numerical stability and minimal acoustic reflections. This approach was subsequently extended to the calculations of Navier-Stokes equations [3, 4], in which the concept of pressure relaxation in the transient boundary conditions was formalized.

The one-dimensional approximation of the characteristic boundary conditions was successfully applied in multi-dimensional Euler equations by Thompson [5, 6]. Poinot and Lele [7] generalized the formulation for the Navier-stokes equations, commonly referred to as the Navier-Stokes characteristic boundary conditions (NSCBC), by including viscous diffusion terms under the locally one-dimensional inviscid (LODI) assumptions. The mathematical well-posedness and stability of the viscous boundary conditions have also been investigated extensively [8-12]. The NSCBC approach was further extended to consider multi-component

reacting flows [13-14], and subsonic nonreflecting inflow conditions were also derived as a variation within the generalized formulation [15].

The extensive list of literature may appear to suggest that the subject of characteristic boundary conditions is by and large a solved problem. In actual simulation practice, however, the existing methods have revealed a variety of numerical difficulties, especially when computing highly turbulent reacting flows. Spurious solution behavior has been observed in many circumstances such as a passing of a strong vortex or a reaction front. Many case-by-case modifications have been proposed in order to alleviate these problems, yet none of them provided a rational and comprehensive remedy to a wide range of flow conditions.

As an example of refinement of the NSCBC approach, Sutherland and Kennedy [16] recognized that the chemical source terms must be considered in the LODI formulation in order to reproduce realistic flame propagation through the boundary. In our recent study of counterflow diffusion flame simulations [17], it was found that transverse convection terms must also be properly accounted for in the modified LODI expression to achieve correct solution behavior. It was also observed that, similar to the pressure relaxation used in the existing nonreflecting boundary conditions, a proper relaxation treatment for the transverse terms was also necessary in order to ensure solution stability. These results suggest that, for a successful application to general turbulent combustion problems, the entire formulation of the characteristic boundary conditions may have to be re-examined for a complete resolution of these issues.

Therefore, the present study attempts to revisit the full NSCBC formulation in a generalized context, by reconsidering many terms that have been neglected before. Improved and generalized LODI approximations that are applicable for a wide range of reacting flow conditions are then derived. As an extension of our previous study [17], a rigorous scaling analysis yields a proper

estimate for the relaxation coefficient appearing in the transverse terms. The proposed boundary conditions are tested under various hostile test problems, such as vortex convection, ignition of a premixed gas mixture, and the Poiseuille flow within a parallel channel, for which the conventional characteristic boundary conditions have been shown to fail. It is demonstrated that the modified boundary conditions provide a systematic and generalized improvement toward robust and stable solution for direct numerical simulations of compressible reacting flows.

## 2. Characteristic boundary conditions

In this section, the basic mathematical formulation is described as a reference to further development of the characteristic boundary condition treatments. The compressible Navier-Stokes, total energy, and species conservation equations for multi-component reacting flows can be transformed into a characteristic form, written as:

$$\frac{\partial}{\partial t} \begin{bmatrix} u \\ v \\ w \\ \rho \\ p \\ Y_i \end{bmatrix} + \begin{bmatrix} (L_5^{(x)} - L_1^{(x)})/\rho c \\ L_3^{(x)} \\ L_4^{(x)} \\ L_2^{(x)} + (L_5^{(x)} + L_1^{(x)})/c^2 \\ L_5^{(x)} + L_1^{(x)} \\ L_{5+i}^{(x)} \end{bmatrix} + \begin{bmatrix} \mathbf{v}_t \cdot \nabla_t u \\ \mathbf{v}_t \cdot \nabla_t v + (1/\rho)\partial p/\partial y \\ \mathbf{v}_t \cdot \nabla_t w + (1/\rho)\partial p/\partial z \\ \mathbf{v}_t \cdot \nabla_t \rho + \rho \nabla_t \cdot \mathbf{v}_t \\ \mathbf{v}_t \cdot \nabla_t p + \gamma p \nabla_t \cdot \mathbf{v}_t \\ \mathbf{v}_t \cdot \nabla_t Y_i \end{bmatrix} = \begin{bmatrix} d_u \\ d_v \\ d_w \\ d_\rho \\ d_p \\ d_{Y_i} \end{bmatrix} + \begin{bmatrix} s_u \\ s_v \\ s_w \\ s_\rho \\ s_p \\ s_{Y_i} \end{bmatrix}, \quad (1)$$

where  $L_k^{(x)}$  are the wave amplitudes of the characteristic variables in  $x$ -direction, subscript  $t$  represents tangential ( $y$  and  $z$ ) directions,  $\mathbf{v}$  is the velocity vector, and  $c = \sqrt{\gamma RT}$  is the speed of sound. We herein used the same definitions of the wave amplitudes  $L_k^{(x)}$ , viscous terms  $d_f$ , and source terms  $s_f$  as in [17].

The system of equation (1) is a generalized form of compressible reacting flows, including the multi-dimensional, viscous, and chemical reaction source terms. In the next section, the conventional LODI approximations are briefly revisited and their pitfalls are discussed.

### 2-1. Conventional LODI relations

The characteristic boundary conditions for multi-dimensional Euler equations was established by Thompson [5, 6], and the formulation has since been extended to the Navier-Stokes equations to include viscous diffusion terms [7, 13-15]. In most of these approaches, the LODI approximation was made to simplify the characteristic wave treatment at the boundary into a one-dimensional form. Based on this assumption, the nonreflecting outflow boundary condition at  $x = l_x$  is given by:

$$L_1^{(x)} = \alpha(p - p_\infty) + L_{1,\text{exact}}^{(x)}, \quad (2)$$

where  $l_x$  is the domain length in the  $x$ -direction,  $p_\infty$  is the target pressure, and

$$\alpha = \sigma c \frac{(1 - Ma^2)}{2l_x} \quad (3)$$

is a pressure relaxation coefficient [3], with  $\sigma$  being the relaxation factor which was set to 0.25 in [7], and  $Ma$  being the maximum Mach number along the boundary.  $L_{1,\text{exact}}^{(x)}$  is the desired steady value of  $L_1^{(x)}$  and depends on the flow configuration [7].

In the original LODI development, all the terms except the first two terms in equation (1) were neglected. In a simple case for which  $L_{1,\text{exact}}^{(x)} = 0$ , equation (2) is then substituted into equation (1) and rearranged to yield the temporal form of the nonreflecting outflow boundary condition:

$$\frac{1}{2} \left( \frac{\partial p}{\partial t} - \rho c \frac{\partial u}{\partial t} \right) = -\alpha(p - p_\infty). \quad (4)$$

The implication of the pressure relaxation term is now clear. In the steady limit where the LHS of equation (4) vanishes, it allows the boundary pressure to smoothly approach the desired target value ( $p \rightarrow p_\infty$ ). It is also clear from equation (4) that this statement is only valid when all the assumptions behind it are valid: that is, only when all the transverse convection, diffusion, and reaction terms are negligible at the boundary. If, on the other hand, any of these terms are not negligible, the generalized form of the temporal form of the nonreflecting outflow boundary condition must be rewritten as [17]:

$$\frac{1}{2} \left( \frac{\partial p}{\partial t} - \rho c \frac{\partial u}{\partial t} \right) = -\alpha(p - p_\infty) + \left( \mathfrak{T}_1^{(x)} + V_1^{(x)} + S_1^{(x)} - L_{1,\text{exact}}^{(x)} \right). \quad (5)$$

For brevity, the above equation will be referred to as the *effective boundary condition*. Here,  $\mathfrak{T}$ ,  $V$ , and  $S$  denote, respectively, the transverse, viscous, and source terms and are given by:

$$\begin{cases} \mathfrak{T}_1^{(x)} = -(\mathbf{v}_t \cdot \nabla_t p + \mathcal{P} \nabla_t \cdot \mathbf{v}_t - \rho c \mathbf{v}_t \cdot \nabla_t u)/2, \\ V_1^{(x)} = (d_p - \rho c d_u)/2, \\ S_1^{(x)} = (s_p - \rho c s_u)/2. \end{cases} \quad (6)$$

Equation (5) demonstrates that, if any of terms in equation (6) becomes significant in magnitude, the boundary pressure approaches an asymptotic value that is different from the desired target value,  $p_\infty$ . This explains the pressure drift and subsequent instability behavior observed in many reacting flow simulations using the conventional LODI approximation. Equation (5) also provides a clue as to how to resolve this problem, as will be discussed in the next section.

## 2-2. Improved boundary condition

We first remark that several previous studies have recognized the significance of the additional terms appearing in the effective boundary condition. For example, Sutherland and Kennedy [16] proposed an inclusion of the reaction source terms in the definition of the wave amplitudes, thereby allowing flames to pass through the boundary without a flow reversal. However, they did not rigorously explain the reason why the reaction source terms must be added in determination of the incoming wave amplitudes. The importance of the transverse terms or the multi-dimensional effect on the boundary conditions was first recognized by Nicoud [18] and Valorani and Favini [19]. However, their studies were based on the Euler equations so that they did not consider any effects of the viscous and reaction source terms in Navier-Stokes equations. More recent studies [20, 21] proposed inflow/outflow boundary conditions for subsonic flows by incorporating transverse, acoustic and viscous effects on the incoming wave, using the low Mach number asymptotics. This approach, however, does not consider the pressure and transverse relaxation terms as employed in the present study, and thus it may suffer from thermodynamic pressure drift in some cases.

Overall, the previous studies do not appear to be able to provide a problem-independent formalism applicable to a broad range of reacting flow conditions. In our previous study [17], this issue has been resolved by introducing a generalized definition of the wave amplitude  $L_1^{(x)}$  at  $x = l_x$  to include the additional terms as:

$$L_1^{(x)} = \alpha(p - p_\infty) + a\mathfrak{T}_{1,\text{exact}}^{(x)} + (1 - a)\mathfrak{T}_1^{(x)} + V_1^{(x)} + S_1^{(x)}, \quad (7)$$

such that the effective boundary condition becomes

$$\frac{1}{2} \left( \frac{\partial p}{\partial t} - \rho c \frac{\partial u}{\partial t} \right) = -\alpha(p - p_\infty) + a(\mathfrak{T}_1^{(x)} - \mathfrak{T}_{1,\text{exact}}^{(x)}), \quad (8)$$



where  $\mathfrak{Z}_{1,\text{exact}}^{(x)}$  is a desired steady value of  $\mathfrak{Z}_1^{(x)}$  in analogy with  $p_\infty$  being the target value for pressure. The additional relaxation term appearing in equation (8) suppresses spurious acoustic waves associated with the transverse convection terms, and was found necessary in order to ensure numerical stability [17].

Similarly, the nonreflecting inflow conditions at  $x = 0$  can be imposed following the same procedure. For example, if the inflow velocity needs to be specified as  $u = u_0$ , we can define:

$$L_5^{(x)} = \beta_5(u - u_0) + \mathfrak{Z}_5^{(x)} + V_5^{(x)} + S_5^{(x)}, \quad (9)$$

where  $\beta_5$  is the  $u$ -velocity relaxation coefficient [17] and the transverse, viscous, and source terms are given by:

$$\begin{cases} \mathfrak{Z}_5^{(x)} = -(\mathbf{v}_t \cdot \nabla_t p + \eta \nabla_t \cdot \mathbf{v}_t + \rho c \mathbf{v}_t \cdot \nabla_t u)/2, \\ V_5^{(x)} = (d_p + \rho c d_u)/2, \\ S_5^{(x)} = (s_p + \rho c s_u)/2. \end{cases} \quad (10)$$

Unlike the outflow boundary conditions, however, we found that the transverse relaxation treatment is not necessary for the inflow conditions as most of the solution variables are specified [17]. Therefore, this paper mainly focuses on the outflow boundary conditions in various test simulations. Note that the improved boundary conditions show they are acoustically transparent in both free stream flow and counterflow tests [17].

It is of interest to note that the generalized effective boundary conditions described above appear to be special cases of the second approximation of Engquist and Majda [1], which is written as

$$\frac{\partial}{\partial t}(\tilde{p} - \bar{\rho} \bar{c} \tilde{u}) + c_1 \tilde{\rho} + c_2 \tilde{u} + c_3 \tilde{v} + c_4 \tilde{p} + c_5 \frac{\partial \tilde{v}}{\partial y} = 0, \quad (11)$$

where “ $-$ ” and “ $\sim$ ” represent, respectively, the steady-state solution and its perturbation, and  $c_i$ ’s are the relaxation coefficients for the corresponding perturbations of solution [3].

In Appendix A, the full description of the inflow and outflow boundary conditions at  $x = 0$  and  $x = l_x$  is summarized. Extension to other spatial directions is straightforward. In the following, the generalized nonreflecting boundary conditions are tested under various test problems, each of which accentuates a situation where some of the additional terms introduced in equation (7) become important. In addition, an asymptotic scaling analysis is performed to derive a rigorous expression for the associated transverse relaxation coefficient,  $a$ .

In this study, we use the same DNS code (S3D) as in our previous study [17]. For reacting test cases, a Hydrogen-Air mechanism developed by Mueller *et al.* [22] is used. Since the body forces are not considered in this study, the source terms in the momentum equations in equation (1) become zero, or  $s_u = s_v = s_w = 0$ . Following Sutherland and Kennedy [16], we specified proper sets of viscous conditions including the diffusive flux conditions for reacting flows, and imposed the correct number of boundary conditions for all the following test cases. Regarding the proper number and forms of the boundary conditions for Euler and Navier-Stoke equations, readers are referred to several previous papers [8, 9, 12, 16].

### 3. Test A: Vortex convection

As a first demonstration of the improved outflow boundary conditions, we start from a nonreacting test case in which a single vortex is convected by the uniform mean flow. Although this problem has been considered in many previous studies [7], most of the existing approaches result in various levels of spurious solution behavior as the vortex passes through the outflow boundary, but it appears that Prosser [21] has resolved the issues encountered in the vortex test

problem. However, we revisit this issue in order to obtain the transverse relaxation coefficient,  $a$ , to clarify the analogy between pressure and transverse relaxation terms, and to demonstrate how solution behaves with the improved boundary conditions. As shown in the previous section, we have identified that the cause of this problem is the presence of strong transverse gradient terms, leading to a large magnitude of extra terms in the effective boundary condition in equation (5). In this section, it will be shown that the modified boundary treatment can resolve this issue successfully.

### 3-1. Determination of the relaxation coefficient

Before the test simulations are performed, we first examine the nature of the problem carefully and then derive an estimate for an appropriate relaxation coefficient,  $a$ , that is needed in the modified boundary conditions, equation (8).

For a 2-D flow, equation (8) is written as:

$$\frac{\partial p}{\partial t} - \rho c \frac{\partial u}{\partial t} = -\frac{\sigma c}{l_x} (p - p_\infty) - a \left( \gamma p \frac{\partial v}{\partial y} + v \frac{\partial p}{\partial y} - \rho c v \frac{\partial u}{\partial y} \right). \quad (12)$$

Note that, since the mean flow is unidirectional,  $\mathfrak{I}_{1,\text{exact}}^{(x)} = 0$ . Following the standard asymptotic analysis for low Mach number flows [23], the following non-dimensional variables are introduced:

$$p^* = p / p_\infty, \quad u^* = u / u_\infty, \quad v^* = v / u_\infty, \quad \rho^* = \rho / \rho_\infty, \quad c^* = c / c_\infty, \\ t^* = t / (l_\infty / u_\infty), \quad x^* = x / l_\infty, \quad y^* = y / l_\infty, \quad (13)$$

$$M = u_\infty / \sqrt{\gamma p_\infty / \rho_\infty},$$

where subscript  $\infty$  represents the reference value. Equation (12) then becomes

$$\frac{\partial p^*}{\partial t^*} - M\gamma\rho^*c^* \frac{\partial u^*}{\partial t^*} = -\frac{\sigma c^*}{Ml_x^*}(p^* - p_\infty^*) - a\left(\mathcal{P}^* \frac{\partial v^*}{\partial y^*} + u^* \frac{\partial p^*}{\partial y^*} - M\gamma\rho^*c^*v^* \frac{\partial u^*}{\partial y^*}\right). \quad (14)$$

For low Mach number flows, which is the main interest of this study, the main dependent variables are expanded in terms of  $M$  as a small parameter, written as:

$$p^* = p_0^* + Mp_1^* + O(M^2), \quad \rho^* = \rho_0^* + M\rho_1^* + O(M^2), \quad \mathbf{v}^* = \mathbf{v}_0^* + M\mathbf{v}_1^* + O(M^2), \quad (15)$$

where  $p_0^*$  and  $p_1^*$  are commonly referred to as the thermodynamic and acoustic pressure, respectively, and  $\mathbf{v}$  is the velocity vector. Substituting equation (15) into (14), and considering that the thermodynamic pressure is steady at  $p_0^* = p_\infty^* = \text{constant}$ , equation (14) becomes

$$M \frac{\partial p_1^*}{\partial t^*} - M\gamma\rho_0^*c_0^* \frac{\partial u_0^*}{\partial t^*} = -M \frac{\sigma c_0^*}{Ml_x^*} p_1^* - a\gamma p_0^* \frac{\partial v_0^*}{\partial y^*} + aM\gamma\rho^*c^*v^* \frac{\partial u_0^*}{\partial y^*} + O(M^2). \quad (16)$$

It is clear from equation (16) that there is only one term,  $a\mathcal{P}_0^* \partial v_0^* / \partial y^*$ , that does not contain the Mach number. Note that this term would normally balance with the streamwise velocity gradient through the leading-order continuity equation in the low Mach number limit:

$$\mathcal{P}_0^* \left( \frac{\partial u_0^*}{\partial x^*} + \frac{\partial v_0^*}{\partial y^*} \right) = 0. \quad (17)$$

However, the  $\partial u_0^* / \partial x^*$  term is absorbed into the pressure relaxation term with the LODI approximation; hence the continuity equation is violated if the transverse gradient term becomes large. Therefore, the proper distinguished limit in the asymptotic expansion suggests that

$$a = M, \quad (18)$$

such that the leading-order equation for equation (16) becomes:

$$\frac{\partial p_1^*}{\partial t^*} - \gamma\rho_0^*c_0^* \frac{\partial u_0^*}{\partial t^*} = -\frac{\sigma c_0^*}{Ml_x^*} p_1^* + \mathcal{P}_0^* \frac{\partial u_0^*}{\partial x^*}, \quad (19)$$

in which the leading-order continuity, equation (17), is used.

The asymptotic analysis implies that the effective boundary condition, equation (12), at leading order can be written as:

$$\frac{\partial p}{\partial t} - \rho c \frac{\partial u}{\partial t} \approx -\frac{\sigma c}{l_x}(p - p_\infty) + \rho c u_\infty \frac{\partial u}{\partial x}, \quad (20)$$

which shows the analogy between the pressure and transverse relaxation terms: they both approximate the time derivative terms as representative spatial derivatives.

For some problems in which the reference Mach number can not be clearly defined, one may be tempted to use the local Mach number as an alternative value in the transverse relaxation coefficient,  $M$ . Equation (20) then becomes

$$\frac{\partial p}{\partial t} - \rho c \frac{\partial u}{\partial t} \approx -\frac{\sigma c}{l_x}(p - p_\infty) + \rho c u \frac{\partial u}{\partial x}, \quad (21)$$

which is similar to the nonreflecting boundary condition proposed by Giles [24], except that the pressure relaxation term was not considered in the condition. However, we found that this alternative approach (both equation (21) and Giles' method) can lead to numerical instability problems, partly because the instantaneous velocity,  $u$ , may vanish or become negative at the boundaries as would happen in general turbulent flow conditions. This issue will be further discussed in Section 4.

### 3-2. Test results

To understand how a vortex interacts with a nonreflecting outflow boundary, a vortex superimposed on a free-stream flow is simulated. The initial vortex is prescribed by:

$$\begin{pmatrix} u \\ v \end{pmatrix} = \begin{pmatrix} u_\infty \\ 0 \end{pmatrix} + 1/\rho \begin{pmatrix} \frac{\partial \psi}{\partial y} \\ -\frac{\partial \psi}{\partial x} \end{pmatrix}, \quad \psi = C \exp\left(-\frac{(x-x_0)^2 + (y-y_0)^2}{2R_c^2}\right). \quad (22)$$

where  $\psi$  is a stream function for an incompressible inviscid vortex,  $C$  is the vortex strength,  $R_c$  is the vortex radius, and  $(x_0, y_0)$  is the location of the vortex center [7]. The initial pressure field corresponding to the vortex is given by:

$$p = p_\infty - \rho \frac{C^2}{R_c^2} \exp\left(-\frac{(x-x_0)^2 + (y-y_0)^2}{2R_c^2}\right). \quad (23)$$

In the test, the flow conditions are specified as:

$$M = u_\infty/c = 0.05, \quad R_c/l_x = 0.1, \quad C/(cl_x) = -0.0025.$$

The domain size is 2.0 mm  $\times$  2.0 mm with 200 grid points in each direction. The reference temperature and pressure are 300 K and 1 atm respectively, and the flow is air. The maximum velocity induced by the vortex is 5.26 m/s. Note that the vortex strength is significantly larger than that tested in Poinso and Lele [7] in order to reveal the errors associated with the previous approaches.

The nonreflecting inflow boundary conditions [17, 25] are adopted at  $x=0$  to suppress acoustic wave reflection at the inflow boundary. For the  $x$ -directional outflow boundary at  $x=l_x$ , four different boundary conditions are considered.

- Case A1 is the conventional LODI approach by Poinso and Lele [7], with  $L_{1,\text{exact}}^{(x)} = 0$ , such that the effective boundary condition thus becomes:

$$\frac{\partial p}{\partial t} - \rho c \frac{\partial u}{\partial t} = -2\alpha(p - p_\infty) + 2(\mathfrak{T}_1^{(x)} + V_1^{(x)} + S_1^{(x)}). \quad (24)$$

- Case A2 includes all the transverse and viscous terms in  $L_1^{(x)}$  and thus the effective boundary condition has only the pressure relaxation term in RHS:

$$\frac{\partial p}{\partial t} - \rho c \frac{\partial u}{\partial t} = -2\alpha(p - p_\infty). \quad (25)$$

- Case A3 is equation (8) with the transverse relaxation coefficient  $a = M = 0.05$  and

$\mathfrak{I}_{1,\text{exact}}^{(x)} = 0$ . The effective boundary condition, equation (8), becomes

$$\frac{\partial p}{\partial t} - \rho c \frac{\partial u}{\partial t} = -2\alpha(p - p_\infty) - 2M\mathfrak{I}_1^{(x)}, \quad (26)$$

For the  $y$ -directional boundaries, the conventional LODI nonreflecting boundary condition (A1) is used to provide the consistent conditions for all test cases. The viscous conditions are  $\partial \tau_{xx} / \partial x = 0$  at  $x = 0$ ,  $\partial q_x / \partial x = 0$ ,  $\partial \tau_{xy} / \partial x = 0$  at  $x = l_x$ , and  $\partial q_y / \partial y = 0$ ,  $\partial \tau_{yx} / \partial y = 0$  at the  $y$ -boundaries.

Figure 1 shows the temporal variations of vorticity isocontours for Cases A1-A3 as the vortex is passing through the outflow boundary. Even if different boundary conditions are used, no significant difference can be found among three cases. At  $t = 56 \mu\text{sec}$ , the center region of the vortex for Cases A1 and A2 are slightly distorted, showing an upward and downward motion at the boundary, respectively. Nevertheless, vorticity is a relatively forgiving metric to assess the solution accuracy as the differences in the four test cases are hardly visible.

On the other hand, the comparison of  $x$ -,  $y$ -velocity, and pressure contours shown through figures 2-4 clearly reveal the numerical artifacts arising from the incorrect boundary condition implementations. For example, Case A1 yields both an acceleration in the  $u$ -velocity and a deceleration in the  $v$ -velocity, while Case A2 leads to an opposite behavior. As a net result, Case A1 shows a tendency to “suck out” the vortex, and Case A2 tends to resist and damp out the vortex.

The pressure isocontours shown in figure 4 reflect the defects in Cases A1 and A2, showing a significant amount of spurious pressure field generation during the vortex-boundary interaction. For Case A1, as the vortex approaches the boundary, the  $\gamma \partial v / \partial y$  term appearing in equation

(24) becomes dominant. Therefore, the effective boundary equation is enforced in the direction to suppress the variation of  $\partial v / \partial y$ , resulting in the unphysical behavior of pressure and velocity fields. On the other hand, Case A2 has only the pressure relaxation term in its effective boundary condition, equation (25), hence the pressure variation is more confined near the boundary with amplitudes smaller than those for Case A1. Since the leading order equation for Case A2 is  $\rho c \partial u / \partial t = 0$ , its net effect is to damp out the  $x$ -velocity near the boundary.

As a more quantitative assessment of the solution accuracy, the L2-norm of the pressure difference is calculated by:

$$\|p(x, y, t) - p_\infty\|_2 / \|p(x, y, 0) - p_\infty\|_2 ,$$

and is monitored in time for the three test cases studied, as shown in figure 5. Cases A1-A2 exhibit a transient burst in the solution error during the early period of the vortex-boundary interaction. In particular, note that Case A2 (a perfect elimination of all the transverse, viscous, and source terms in the effective boundary conditions) leads to an inaccurate steady-state solution in the pressure field. As explained earlier, Nicoud [18] recognized this issue and suggested an inclusion of some types of transverse terms similar to those in equations (24) and (26), but no definitive resolution was reported. In contrast, Case A3 shows no such artifacts and yields a clean decay in the pressure difference variation at substantially smaller values. This presents clear evidence of the superiority of the proposed boundary conditions compared to conventional LODI approaches.

With the successful demonstration of the improved boundary conditions (Case A3), this approach has also been tested in flows with different Mach numbers. The conditions are the same as those in the previous tests except the mean velocity (and  $a = M$ ). Figure 6 shows the L2-norms of the pressure difference for different Mach number conditions. All test cases yield monotonic



decay of the pressure difference without any spurious burst. It is of interest to note that the “bumps” in the pressure difference around at 0.7-1.0 flow time in figure 6 becomes noticeable as the mean flow velocity increases. This is because the assumption for low Mach number flows is not perfectly valid and thus the proposed boundary condition may not be ideal for high Mach number flow cases. Nevertheless, even these anomalies with the improved boundary conditions are almost 2 orders of magnitude smaller than those from other approaches (see figure 5). Therefore, this result confirms that the value of  $a$  derived from the low Mach number expansion is appropriate for a wide range of subsonic flow conditions compared to other boundary conditions.

From the results, it is confirmed that the improved boundary conditions, Case A3, with a properly chosen relaxation coefficient,  $a$ , accurately reproduce transient solution behavior at the boundary and achieve rapid convergence to a steady solution.

#### 4. Test B: Turbulent flow

To confirm the validity of the improved boundary conditions in general unsteady flow conditions, we next consider a turbulent inflow in a free stream flow. The test domain size is  $10 \text{ mm} \times 5 \text{ mm}$  with  $400 \times 200$  grid points. The calculation conditions are specified as:

$$M = u_\infty / c = 0.05, \quad L_{11} / l_y = 0.05, \quad u' / u_\infty = 0.15,$$

where  $L_{11}$  and  $u'$  are, respectively, the turbulence integral length scale and turbulence intensity. For turbulence injection at the inflow boundary, the unsteady nonreflecting inflow conditions are used to impose prescribed turbulent inflow conditions [17]. The imposed inlet velocities at  $x = 0$  are given by  $u_0(y, t) = u_\infty + u'_0(y, t)$  and  $v_0(y, t) = v'_0(y, t)$ , where  $u'_0(y, t)$  and  $v'_0(y, t)$  are the turbulent fluctuation velocities, which are obtained from an auxiliary homogeneous isotropic

turbulent flow field generated at the start of the simulation. The fluctuation velocities,  $u'_0$  and  $v'_0$  correspond to the velocities of a one-dimensional slice of the two-dimensional turbulent flow field at a given location,  $u_\infty \cdot t$  from the Taylor hypothesis [26].

Four different nonreflecting boundary conditions similar to those discussed in the previous section were tested. For each test case, the identical conditions are applied at all three outflow boundaries.

- Case B1 uses the conventional LODI boundary condition as in Case A1
- Case B2 uses the boundary condition in Case A2
- Case B3 uses the improved boundary conditions with  $a = M = 0.05$  and  $\mathfrak{Z}_{\text{l,exact}}^{(x)} = 0$  as in Case A3.  $a = M = 0.05$  is also used for the y-directional outflow boundary conditions
- Case B4 used the improved boundary condition with the local Mach number as the transverse relaxation coefficient,  $a$ .

Figure 7 shows the temporal variations of (a) the minimum pressure and (b) the L2-norm of pressure difference. Among the four conditions tested, Cases B2 and B4 suffer from numerical instability at an early stage of simulation. As discussed in Section 3-1, these two cases that do not consider the transverse relaxation are found inadequate for turbulent flow simulations. Between Cases B1 and B3, Case B3 shows much smaller pressure variations and the L2-norm of pressure difference. Therefore, it is confirmed that the improved boundary condition provides more robust and accurate solutions for turbulent flow conditions. It is of interest to note that the large pressure variation in Case B1 occurs at the corners of the domain. We suspect it comes from the “corner problem” due to unmatched boundary conditions [27].

With the asymptotic scaling to determine the transverse relaxation coefficients, we have also revisited the counterflow simulation considered in our previous study [17] and refined the

solution stability and accuracy. While this is rather a subtle issue, the discussion of the revised boundary conditions for the nonreacting counterflow with high flow velocities is provided in Appendix B for completeness.

## **5. Test C: Ignition of homogeneous reactant mixture**

The previous test cases demonstrated the importance of considering the transverse convective terms in equation (7), in order to suppress their adverse effects on the boundary treatment. The next test case represents a situation in which the source term,  $S_1$ , in equation (7) becomes important and must be taken into account. For this purpose, we adopt the ignition of a homogeneous reactant mixture by a temperature peak. In a similar configuration, Sutherland and Kennedy [16] found that flow reversals occur when flame passes through a nonreflecting boundary. They recognized the importance to include the reaction source terms in the corresponding wave amplitudes and demonstrated an improvement in the solution behavior. However, their improved solutions still showed that the flame becomes square-shaped as it approaches the boundaries. In this section, this issue is revisited and further improvement is sought.

### *5-1. Test results*

Unlike the vortex-convection test, the transverse relaxation coefficient  $a$  cannot be determined simply by the low Mach number expansion. This is because (a) there is no specific Mach number based on the mean flow condition, and (b) the thermodynamic pressure is not constant but varies in time and space during the ignition process. For this particular test case, however, the local normal velocity at the boundaries remain positive at all times, hence we use

the local Mach number in determining the transverse relaxation coefficient without causing numerical instability.

The test configuration is a 2D square domain with a dimension of  $2.0 \text{ mm} \times 2.0 \text{ mm}$  and  $200 \times 200$  grid resolution. The initial condition is a stoichiometric  $\text{H}_2/\text{O}_2$  mixture diluted with 50 %  $\text{N}_2$  by volume at 300 K and 1.0 atm. To ignite the mixture, a Gaussian temperature peak at the maximum temperature of 2100 K is superimposed at the center of the domain.

As in the vortex convection test, the flow field induced by the circular ignition front generates significant tangential velocity gradients at the boundaries. Therefore, without a proper consideration of the transverse terms in the wave amplitude expression, an acceleration in the normal flow velocity near the center region of the boundaries, similar to the observation in figure 3 for Case A1. This is attributed to the main cause for the square-shaped ignition front observed in [16].

To demonstrate further improvements made by the boundary conditions in the present study, three different cases were tested.

- Case C1 uses the conventional LODI boundary condition (as in Case A1) with  $L_{1,\text{exact}}^{(x)} = 0$ ,
- Case C2 includes only the reaction source terms in the corresponding incoming  $L_k$ 's, as proposed by Sutherland and Kennedy [16]. For example, the effective outflow boundary condition at  $x = l_x$  is given by:

$$\frac{1}{2} \left( \frac{\partial p}{\partial t} - \rho c \frac{\partial u}{\partial t} \right) = -\alpha(p - p_\infty) + (\mathfrak{I}_1^{(x)} + V_1^{(x)}), \quad (27)$$

- Case C3 is the improved boundary conditions with  $a$  being the local Mach number and  $\mathfrak{I}_{1,\text{exact}}^{(x)} = 0$ .

In all cases, the viscous conditions are imposed as  $\partial q_x / \partial x = 0$ ,  $\partial(\rho Y_i V_{i,x}) / \partial x = 0$ ,  $\partial \tau_{xy} / \partial x = 0$  at the  $x$ -boundaries and  $\partial q_y / \partial y = 0$ ,  $\partial(\rho Y_i V_{i,y}) / \partial y = 0$ ,  $\partial \tau_{yx} / \partial y = 0$  at the  $y$ -boundaries.

Figure 8 shows the temporal variations of temperature isocontours for Cases C1–C3 at  $t = 12$ , 18, 22, and 27  $\mu\text{sec}$ . Figure 9 shows the corresponding velocity field and the  $\text{HO}_2$  mass fraction isocontour in order to indicate the ignition front location. It is clearly seen that Case C1, which neglects both transverse and reaction source terms, results in a severe flow reversal as the ignition front passes through the boundaries. For Case C2, with consideration of the reaction source, the problems of the flow reversal and pressure increase are significantly reduced. However, the neglect in the transverse term effect results in a normal flow acceleration in the center part of the boundaries, leading to a square-shaped front. Finally, Case C3, with full consideration of all the relevant terms in the wave amplitude, exhibits correct behavior of a circular front propagation. However, a slight flow deceleration is observed in Case C3, which may be attributed to that the pressure relaxation force is larger than expected and thus the transverse relaxation does not work effectively. An alternative interpretation is that an excessively large  $\sigma$  leads to the leading order equation in equation (14) to be  $\sigma c^* / Ml_x^* \cdot (p_0^* - p_\infty^*) = 0$ , which implies that the pressure at the boundary is forced to maintain the imposed value too strictly. This effect further contributes to the square shape in the ignition front regardless of the transverse relaxation term.

## 6. Test D: The Poiseuille flow

As the last class of test cases, we consider a laminar flow between two parallel plates. The Poiseuille flow represents an excellent example where the viscous terms become important at the

boundaries. In this section, a proper form of the no-slip wall boundary conditions is discussed and improved boundary conditions are tested in conjunction with various nonreflecting outflow boundary conditions. Both nonreacting and reacting flow conditions are tested to demonstrate the wide applicability of the new boundary conditions.

#### 6-1. Wall boundary conditions

For a bounded flow in a channel, the no-slip conditions implies a straightforward velocity boundary conditions,  $u = v = w = 0$ , at the wall for the momentum equations. For the energy equation, we may directly specify temperature at an isothermal wall,  $T = T_{\text{wall}}$  or heat flux at wall,  $\mathbf{n} \cdot \mathbf{q} = q_{\text{wall}}$ , where  $\mathbf{n}$  denotes the unit normal vector with respect to the boundary surface. Similarly, the boundary conditions for the species variables can be specified as  $\rho Y_i (\mathbf{n} \cdot \mathbf{V}_i) = \rho Y_i \mathbf{V}_{i,n} = 0$  for impermeable walls, where subscript  $n$  denotes the normal direction.

On the other hand, the boundary conditions for the continuity equations have been treated in a number of different ways [2, 7, 28, 29]. Both Thompson [2] and Poinso and Lele [7] specified the  $L_k$  values as boundary conditions using the LODI assumptions. In doing so, however, they overspecified the boundary conditions and ignored the viscous effect at the wall.

As an alternative approach, Kennedy [28] and Hirsch [29] derived a boundary condition using the material derivative of the impermeability condition:

$$\rho \frac{D(\mathbf{u} \cdot \mathbf{n})}{Dt} = \rho \mathbf{u} \cdot \frac{D\mathbf{n}}{Dt} + \rho \frac{D\mathbf{u}}{Dt} \cdot \mathbf{n} = 0, \quad (28)$$

Since we consider only the Cartesian coordinates, the normal vector is independent of time and space and the material derivative of the normal vector in equation (28) thus vanishes.

Substituting the momentum equation into equation (28), the boundary condition for the continuity equation can be obtained as:

$$(\mathbf{n} \cdot \nabla)p = (\nabla \cdot \boldsymbol{\tau}) \cdot \mathbf{n}. \quad (29)$$

Instead of directly specifying equation (29) for the continuity equation, we devise a way to determine  $L_1^{(n)}$  and  $L_5^{(n)}$  values by combining equation (31) with  $L_k^{(n)}$ . As explained above, Thompson and Poinso, and Lele specified  $L_1^{(n)} = L_5^{(n)}$ , or vice versa depending on the wall location, by ignoring the viscous terms in the momentum equation. In reality, however, the viscous terms are not negligible at the wall and hence must be properly accounted for. Considering the viscous terms in the momentum equation,  $L_1^{(n)}$  is given by:

$$L_1^{(n)} = L_5^{(n)} - c(\nabla \cdot \boldsymbol{\tau}) \cdot \mathbf{n}. \quad (30)$$

During the calculation,  $L_1^{(n)}$  always appears with  $L_5^{(n)}$  in the continuity equation (see equation (1)). Thus, combining equations (29) and (30), one may obtain  $L_1^{(n)} + L_5^{(n)}$  as:

$$L_1^{(n)} + L_5^{(n)} = 2L_5^{(n)} - c(\nabla \cdot \boldsymbol{\tau}) \cdot \mathbf{n} = \rho c^2 (\nabla_n \cdot \mathbf{v}) + c((\mathbf{n} \cdot \nabla)p - (\nabla \cdot \boldsymbol{\tau}) \cdot \mathbf{n}) = \rho c^2 (\nabla \cdot \mathbf{v})_n. \quad (31)$$

In the code, the two characteristic amplitudes,  $L_1^{(n)}$  and  $L_5^{(n)}$  can be specified as  $L_1^{(n)} = 0$  and  $L_5^{(n)} = \rho c^2 (\nabla_n \cdot \mathbf{v})$ , or vice versa, because only the sum of the two is needed in the actual calculation. Therefore, the final forms of the boundary conditions for a bounded flow are given by:

$$\begin{cases} L_1^{(n)} + L_5^{(n)} = \rho c^2 (\nabla_n \cdot \mathbf{v}), \\ u = v = w = 0, \\ T = T_{\text{wall}} \text{ or } \mathbf{n} \cdot \mathbf{q} = q_{\text{wall}}, \\ \rho Y_i (\mathbf{n} \cdot \mathbf{V}_i) = 0. \end{cases} \quad (32)$$

## 6-2. Test results: nonreacting Poiseuille flow

With the implementation of correct wall boundary conditions, equation (32), we now test the effects of various outflow boundary conditions. Since the viscous terms in the Poiseuille flow becomes important, it is expected that these terms must be considered in the corresponding outflow boundary condition as seen in equation (5). As a model problem, we adopt a 2-D nonreacting laminar flow between two parallel plates. The domain size is  $10 \text{ mm} \times 2 \text{ mm}$  with  $200 \times 50$  grid resolution. The initial velocity field throughout the entire domain is given as a fully-developed velocity profile:

$$u(y) = u_{\max} \left(1 - (y/b)^2\right) \text{ and } v = 0, \quad (33)$$

where  $u_{\max}$  is the maximum velocity on the axis and  $b$  is the half-width. The Reynolds number is  $\text{Re} = u_{\max} b / \nu = 15$  and the Mach number of the flow is  $M = u_{\max} / c = 0.1$ , where  $\nu$  is the kinematic viscosity. The initial temperature and pressure are 300 K and 1.0 atm, respectively.

To demonstrate why the viscous terms must be considered at the outflow boundary, three different cases were tested.

- Case D1 uses the conventional LODI boundary condition as in Case A1 with

$$L_{1,\text{exact}}^{(x)} = (u - c) / 2 \cdot \partial p_{\text{steady}} / \partial x$$

- Case D2 uses the boundary condition as in Case A2,
- Case D3 uses the improved boundary condition with  $a = M = 0.1$  and  $\mathfrak{I}_{1,\text{exact}}^{(x)} = 0$ .

For all the cases above, the inflow boundary condition is the hard inflow condition which directly specifies the solution variables  $\{u, v, w, T, Y_i\}$  at  $x = 0$ , and the isothermal no-slip wall conditions as in equation (32) are applied to the y-directional boundaries. The viscous conditions



are  $\partial\tau_{xx}/\partial x_x = 0$  for the inflow boundary, and  $\partial q_x/\partial x_x = 0$ ,  $\partial\tau_{xy}/\partial x_x = 0$  for the outflow boundary.

Figure 10 shows the temporal variations of the maximum and minimum pressure for Cases D1–D3. Two points are noted in figure 10. First, for Case D1, it takes a much longer time for pressure to reach the steady state than those in other cases. Second, the steady pressure values in Case D1 are larger than those in other cases. It is shown that the minimum pressure in Case D1 increases up to 1.006 atm even if the imposed pressure at the outflow boundary is 1.0 atm. This implies that the estimated  $L_{1,\text{exact}}^{(x)}$  does not perfectly remove the effect of  $V_1^{(x)}$  from the effective boundary condition, equation (5). The same problem has been found in Section 6 of Poinso and Lele [7], in which the pressure at the outflow boundary of the conventional LODI denoted by “B3” (in [7]) is less than the imposed value,  $p_\infty$ , suggesting that  $L_{1,\text{exact}}^{(x)}$  is not correctly estimated.

Figure 11 further shows the steady pressure isocontours for Cases D1–D3. It is confirmed that the pressure at the outflow boundary of Case D1 is larger than the imposed value and the pressure fields of Cases D2–D3 are almost identical even if the minimum pressure in Case D2 is slightly less than those in Cases D3.

Comparing only the steady pressure fields in Cases D1–D3, the corresponding boundary conditions for Cases D2–D3 may appear to be sufficiently accurate for the Poiseuille flow. However, comparison of the  $y$ -directional velocity reveals significant discrepancies, as shown in figure 12. Comparing the steady  $v$ -velocity fields, it is found that relatively large velocities are induced at the outflow boundary for Case D2. The unphysical  $y$ -velocity behavior is consistent with our observations in Section 3-2.

From the results, it is concluded that the consideration of the viscous terms,  $V_1^{(x)}$ , in  $L_1^{(x)}$  is essential in achieving accurate solutions when their magnitude at the boundary is significant. The proposed new boundary conditions also show a better convergence rate compared to other previous LODI approaches.

### 6-3. Test results: reacting Poiseuille-flow

The improved boundary conditions are now applied to a channel flow in the presence of chemical reaction and flame propagation in the gas-phase. For a 2-D reacting channel flow calculation, we use the adiabatic no-slip wall conditions as in equation (32) for the two wall boundaries, the hard inflow condition for inflow boundary, and the improved boundary condition for outflow boundary. Using the PREMIX code [30], the velocity, temperature, and species profiles of 1-D stoichiometric H<sub>2</sub>-air premixed flame are obtained and mapped into the uniform grid in the 2-D channel. A flat flame is initially located at the center of the channel. The initial  $u$  and  $v$  are assumed to be fully developed and thus are given by equation (35) in which  $u_{\max}$  is imposed as the 1-D flame speed. The domain size is 10 mm  $\times$  2 mm with 200  $\times$  100 grid resolution. The inlet temperature and initial pressure are respectively 300 K and 1.0 atm. The viscous conditions for inflow/outflow boundaries are the same as in Section 6-2 and zero normal gradient of diffusive flux condition  $\partial(\rho Y_i V_{i,x})/\partial x = 0$  is also used at the outflow boundaries.

With the above boundary and initial conditions, we can successfully obtain a solution of the premixed H<sub>2</sub>-air flame in the 2-D channel. Figure 13 shows the temperature,  $Y_{\text{HO}_2}$ ,  $u$  and  $v$  isocontours at  $t = 1.0$  msec. Even if the two no-slip walls and hard inflow boundary behave as reflecting boundaries for acoustic waves, no evident numerical artifacts are visible at all

boundaries. Therefore, it is confirmed that the improved boundary conditions can be successfully applied to reacting and nonreacting channel flow simulations.

## 7. Concluding Remarks

A generalized formulation for the characteristic boundary conditions has been developed for compressible flow equations in the presence of multi-dimensional flow, viscous, and reaction effects. Compared to the many existing approaches, the main features of the present formulation include a proper consideration of additional terms in the definition of the characteristic wave amplitudes, and the relaxation treatment for the transverse gradient terms in analogy with the pressure relaxation employed in previous studies.

From the low Mach number expansion, the appropriate transverse relaxation coefficient,  $a$ , was found to be equal to the corresponding mean flow Mach number. It was demonstrated that the improved boundary conditions work effectively also in a number of test problems including vortex convection, turbulent inflow, and counterflow configurations. For the ignition case, the improved boundary conditions with  $a$  determined by the local Mach number were found to be an excellent remedy for the unphysical square-shaped ignition fronts observed in previous studies. The improved boundary conditions were also applied to the Poiseuille flow configurations in which the viscous effect becomes significant. Combined with a newly-proposed set of the wall boundary conditions, it was demonstrated that the reacting and nonreacting channel flow simulations were successfully performed without numerical artifacts at the boundaries.

For all the test cases, it was found that the transverse relaxation terms with a properly determined relaxation coefficient play a crucial role in ensuring stable solution behavior for

highly transient flows. It is anticipated that the proposed characteristic boundary conditions allow robust and accurate simulations of turbulent reacting flows in various configurations.

### **Acknowledgments**

This work was supported by the Department of Energy, Office of Basic Energy Science, SciDAC Computational Chemistry Program.

## Appendix A. Subsonic nonreflecting inflow/outflow boundary conditions

The subsonic nonreflecting inflow/outflow boundary conditions in the  $x$ -direction are summarized in Tables 1 and 2, which are followed by the corresponding transverse, viscous, and source terms in Table 3.

Table 1. Subsonic nonreflecting inflow boundary conditions in the  $x$ -direction ( $\beta_k$  are the relaxation coefficients corresponding to scalar variables such as  $u$ ,  $v$ ,  $w$ ,  $T$ , and  $Y_i$ , see Ref [17])

Subsonic inflow $u > 0$ at $x = 0$		Subsonic inflow $u < 0$ at $x = l_x$	
Wave velocity	$L_k^{(x)}$ at $x = 0$	Wave velocity	$L_k^{(x)}$ at $x = l_x$
$u - c < 0$	$L_1^{(x)}$ computed	$u - c < 0$	$L_1^{(x)} = \beta_1(u - u_{l_x}) + \mathfrak{T}_1^{(x)} + V_1^{(x)} + S_1^{(x)}$
$u > 0$	$L_2^{(x)} = \beta_2(T - T_0) + \mathfrak{T}_2^{(x)} + V_2^{(x)} + S_2^{(x)}$	$u < 0$	$L_2^{(x)} = \beta_2(T - T_{l_x}) + \mathfrak{T}_2^{(x)} + V_2^{(x)} + S_2^{(x)}$
$u > 0$	$L_3^{(x)} = \beta_3(v - v_0) + \mathfrak{T}_3^{(x)} + V_3^{(x)} + S_3^{(x)}$	$u < 0$	$L_3^{(x)} = \beta_3(v - v_{l_x}) + \mathfrak{T}_3^{(x)} + V_3^{(x)} + S_3^{(x)}$
$u > 0$	$L_4^{(x)} = \beta_4(w - w_0) + \mathfrak{T}_4^{(x)} + V_4^{(x)} + S_4^{(x)}$	$u < 0$	$L_4^{(x)} = \beta_4(w - w_{l_x}) + \mathfrak{T}_4^{(x)} + V_4^{(x)} + S_4^{(x)}$
$u + c > 0$	$L_5^{(x)} = \beta_5(u - u_0) + \mathfrak{T}_5^{(x)} + V_5^{(x)} + S_5^{(x)}$	$u + c > 0$	$L_5^{(x)}$ computed
$u > 0$	$L_{5+i}^{(x)} = \beta_{5+i}(Y_i - Y_{i,0}) + \mathfrak{T}_{5+i}^{(x)} + V_{5+i}^{(x)} + S_{5+i}^{(x)}$	$u < 0$	$L_{5+i}^{(x)} = \beta_{5+i}(Y_i - Y_{i,l_x}) + \mathfrak{T}_{5+i}^{(x)} + V_{5+i}^{(x)} + S_{5+i}^{(x)}$

Table 2. Subsonic nonreflecting outflow boundary conditions in the  $x$ -direction

Subsonic outflow $u < 0$ at $x = 0$		Subsonic outflow $u > 0$ at $x = l_x$	
Wave velocity	$L_k^{(x)}$ at $x = 0$	Wave velocity	$L_k^{(x)}$ at $x = l_x$
$u - c < 0$	$L_1^{(x)}$ computed	$u - c < 0$	$L_1^{(x)} = \alpha(p - p_\infty) + (1 - a)\mathfrak{T}_1^{(x)} + a\mathfrak{T}_{1,\text{exact}}^{(x)} + V_1^{(x)} + S_1^{(x)}$
$u < 0$	$L_2^{(x)}$ computed	$u > 0$	$L_2^{(x)}$ computed
$u < 0$	$L_3^{(x)}$ computed	$u > 0$	$L_3^{(x)}$ computed
$u < 0$	$L_4^{(x)}$ computed	$u > 0$	$L_4^{(x)}$ computed
$u + c > 0$	$L_5^{(x)} = \alpha(p - p_\infty) + (1 - a)\mathfrak{T}_5^{(x)} + a\mathfrak{T}_{5,\text{exact}}^{(x)} + V_5^{(x)} + S_5^{(x)}$	$u + c > 0$	$L_5^{(x)}$ computed
$u < 0$	$L_{5+i}^{(x)}$ computed	$u > 0$	$L_{5+i}^{(x)}$ computed

Table 3. Transverse, viscous, and source terms in the  $x$ -direction (subscript  $t$  denotes the  $y$ - and  $z$ -directions)

$\mathfrak{I}_k^{(x)}$	$V_k^{(x)}$	$S_k^{(x)}$
$\mathfrak{I}_1^{(x)} = -(\mathbf{v}_t \cdot \nabla_t p + \eta \nabla_t \cdot \mathbf{v}_t - \rho c \mathbf{v}_t \cdot \nabla_t u)/2$	$V_1^{(x)} = (d_p - \rho c d_u)/2$	$S_1^{(x)} = (s_p - \rho c s_u)/2$
$\mathfrak{I}_2^{(x)} = -\nabla_t \cdot (\rho \mathbf{v}_t) + (\mathbf{v}_t \cdot \nabla_t p + \eta \nabla_t \cdot \mathbf{v}_t)/c^2$	$V_2^{(x)} = d_\rho - d_p/c^2$	$S_2^{(x)} = s_\rho - s_p/c^2$
$\mathfrak{I}_3^{(x)} = -(\mathbf{v}_t \cdot \nabla_t v + (1/\rho) \partial p / \partial y)$	$V_3^{(x)} = d_v$	$S_3^{(x)} = s_v$
$\mathfrak{I}_4^{(x)} = -(\mathbf{v}_t \cdot \nabla_t w + (1/\rho) \partial p / \partial z)$	$V_4^{(x)} = d_w$	$S_4^{(x)} = s_w$
$\mathfrak{I}_5^{(x)} = -(\mathbf{v}_t \cdot \nabla_t p + \eta \nabla_t \cdot \mathbf{v}_t + \rho c \mathbf{v}_t \cdot \nabla_t u)/2$	$V_1^{(x)} = (d_p + \rho c d_u)/2$	$S_5^{(x)} = (s_p + \rho c s_u)/2$
$\mathfrak{I}_{5+i}^{(x)} = -\mathbf{v}_t \cdot \nabla_t Y_i$	$V_{5+i}^{(x)} = d_{Y_i}$	$S_{5+i}^{(x)} = s_{Y_i}$

## Appendix B. Test E: Nonreacting counterflow

We revisit the 2-D counterflow case considered in our previous study [17] with the newly-proposed relaxation coefficient  $a$ . Consider a nonreacting counterflow configuration in which flow comes in from the two  $x$ -boundaries and leaves through the two  $y$ -boundaries such that the initial pressure is given by the potential flow solution:

$$p_p = p_0 + \frac{1}{2} \rho_0 (u_0^2 + v_0^2) - \frac{1}{2} \rho_0 (u_p(x)^2 + v_p(y)^2), \quad (\text{B1})$$

and the velocities are given by:

$$u_p(x) = -\kappa(x - l_x/2) \text{ and } v_p(y) = \kappa(y - l_y/2), \quad (\text{B2})$$

where subscript 0 denotes the reference value and  $\kappa$  [1/s] is strain rate. Choosing the upper left corner of the domain as the reference point, the imposed pressure at the  $y$ -boundaries is given by:

$$p_{\text{target}} = p_0 - \frac{1}{2} \rho_0 (u_p^2 - u_0^2). \quad (\text{B3})$$

In our previous study [17], the transverse relaxation coefficient,  $a$ , was determined to be 0.01 by trial and error. While the steady counterflow field was successfully reproduced with this method,

it was further identified that the solution becomes unstable as the inlet velocity becomes large, typically exceeding 30 m/s.

From the definition of  $L_1^{(y)}$  and  $L_5^{(y)}$ , and the potential flow assumption in equations (B1)–(B2),  $L_{1,\text{exact}}^{(y)}$  and  $L_{5,\text{exact}}^{(y)}$  for the LODI boundary conditions are specified as:

$$L_{1,\text{exact}}^{(y)} = L_{5,\text{exact}}^{(y)} \approx (c_0^2 - v_0^2) \cdot (\rho_0 v_0 / l_y). \quad (\text{B4})$$

If density is assumed constant, the effective equation for the LODI boundary condition at  $y = l_y$  becomes:

$$\alpha(p - p_{\text{target}}) - (\mathfrak{I}_1^{(y)} + V_1^{(y)} + S_1^{(y)} - L_{1,\text{exact}}^{(y)}) = 0. \quad (\text{B5})$$

For simplicity, consider a square domain such that  $l_x = l_y = l$ . Since it is assumed that  $u_0 = v_0 = v$ ,  $\partial v / \partial y = 2v_0 / l$ ,  $\partial p / \partial y = -\rho_0 v \partial v / \partial y$ , and  $\mathfrak{I}_1^{(y)} + V_1^{(y)} + S_1^{(y)} = L_1^{(y)}$  at the steady state, equation (B5) becomes

$$\alpha \left[ p - \left( p_0 - \frac{1}{2} \rho (u_p^2 - u_0^2) \right) \right] - \left[ (c^2 - v_0^2) \frac{\rho_0 v_0}{l} - (c_0^2 - v_0^2) \frac{\rho_0 v_0}{l} \right] \approx 0, \quad (\text{B6})$$

Since  $\rho_0 c^2 = \mathcal{P}$  and  $\rho_0 c_0^2 = \mathcal{P}_0$ , the steady pressure is thus given by:

$$p \approx p_0 - \frac{1}{2} \rho_0 k (u_p^2 - u_0^2) \quad \text{and} \quad k \equiv (1 - \mathcal{P}_0 / \mathcal{P})^{-1}. \quad (\text{B7})$$

With a small inlet velocity,  $k$  is close to 1.0 so that the steady pressure approaches the target value as in equation (B3). However, as the inlet velocity is increased,  $k$  has positive, zero, and negative values progressively. This implies that the pressure field cannot follow the imposed values for large inlet velocity, leading to an inaccurate solution and numerical instability. In particular, when  $k$  has a negative value, pressure may become inverted (that is, pressure at the center of the domain becomes lowest).

We can easily estimate when the instability would occur due to the pressure inversion. Based on the condition for air, we obtain:

$$u_0 \geq \frac{\sigma c}{2\gamma} = \frac{0.25 \cdot 347}{2 \cdot 1.4} \approx 30 \text{ m/s}.$$

This estimate explains why a steady counterflow with  $u_0 = 30 \text{ m/s}$  could not be obtained in the previous study [17]. As the inlet velocity is increased, the transverse terms in the outflow also increase while the pressure remains constant regardless of the inlet velocity. Consequently, above a certain critical point, the transverse terms become larger than the pressure relaxation term, resulting in numerical instability. On the other hand, if the value of  $a$  is properly chosen to scale with the Mach number, the solution does not suffer from instability due to the pressure inversion.

#### *B-1. Test case*

Since the steady counterflows were already tested for several situations in the previous study [17], nonreacting turbulent counterflow cases are simulated with the appropriate relaxation coefficient  $a$ . The domain size is  $5.0 \text{ mm} \times 5.0 \text{ mm}$  with 200 grid points in each direction. The calculation conditions are specified as:

$$M = u_0/c_0 = 0.05, \quad L_{11}/l_y = 0.1, \quad u'/u_0 = 0.2.$$

For the  $x$ -directional boundaries, the unsteady nonreflecting inflow conditions are used to impose prescribed turbulent inflow conditions [17]. The viscous conditions are  $\partial\tau_{xx}/\partial x = 0$  at the  $x$ -boundaries, and  $\partial q_y/\partial y = 0$ ,  $\partial\tau_{yx}/\partial y = 0$  at the  $y$ -boundaries.

To compare different boundary conditions, three different cases are tested.



- Case E1 uses the conventional LODI boundary condition with

$$L_{1,\text{exact}}^{(y)} = L_{5,\text{exact}}^{(y)} = (c_0^2 - v_0^2) \cdot (\rho_0 v_0 / l_y)$$

- Case E2 uses the boundary condition as in A2,
- For Case E3, the improved boundary condition is used with  $a = 0.05$  and

$$\mathfrak{I}_{1,\text{exact}}^{(y)} = (c_0^2 - u_p^2) \cdot (\rho_0 u_0 / l_x).$$

Figure 14 shows the temporal variations of (a) the minimum pressure and (b) the L2-norm of pressure difference normalized by the potential pressure value for Cases E1–E3, calculated by:

$$\|p(x, y, t) - p_p(x, y)\|_2 / \|p_p(x, y)\|_2.$$

Note that the solution in Case E2 fails at  $t = 0.56$  msec. As in Section 4, we confirm that the nonreflecting boundary condition without velocity relaxation term has an inherent instability problem. For Case E1, the minimum pressure varies by up to 15% of its steady values, implying that the conventional LODI boundary conditions fail in turbulent counterflow configurations. For Case E3, the pressure and L2-norm of pressure difference variations show stable and accurate solution behavior.

## References

- [1] Engquist, E. and Majda, A., 1977, Absorbing boundary conditions for the numerical simulation of waves, *Mathematics of Computation*, **31**, 629-651.
- [2] Hedstrom, G.W., 1979, Non-reflecting boundary conditions for nonlinear hyperbolic systems, *Journal of Computational Physics*, **30**, 222-237.
- [3] Rudy, D.H. and Strikwerda, J.C., 1980, A non-reflecting outflow boundary condition for subsonic Navier-Stokes calculations, *Journal of Computational Physics*, **36**, 55-70.
- [4] Rudy, D.H. and Strikwerda, J.C., 1981, Boundary Conditions for Subsonic Compressible Navier-Stokes Calculations, *Computers and Fluids*, **9**, 327-338.
- [5] Thompson, K.W., 1987, Time-dependent boundary conditions for hyperbolic systems, *Journal of Computational Physics*, **68**, 1-24.
- [6] Thompson, K.W., 1990, Time-dependent boundary conditions for hyperbolic systems II, *Journal of Computational Physics*, **89**, 439-461.
- [7] Poinso, T.J. and Lele, S.K., 1992, Boundary conditions for direct simulations of compressible viscous flows, *Journal of Computational Physics*, **101**, 104-139.
- [8] Strikwerda, J.C., 1977, Initial boundary-value problems for incompletely parabolic systems, *Communication on Pure and Applied Mathematics*, **9**, 797-822.
- [9] Gustafsson, B. and Sundström, A., 1987, Incompletely parabolic problems in fluid-dynamics, *SIAM Journal on Applied Mathematics*, **35**, 343-357.
- [10] Olinger, J. and Sundström, A., 1978, Theoretical and practical aspects of some initial boundary-value problems in fluid-dynamics, *SIAM Journal on Applied Mathematics*, **35**, 419-446.

- [11] Halpern, L., 1991, Artificial boundary conditions for incompletely parabolic perturbations of hyperbolic systems, *SIAM Journal on Mathematical Analysis*, **22**, 1256-1283.
- [12] Dutt, P., 1988, Stable boundary conditions in and difference schemes for Navier-Stokes equations, *SIAM Journal on Numerical Analysis*, **25**, 245-267.
- [13] Baum, M., Poinso, T.J. and Thévenin, D., 1994, Accurate boundary conditions for multi component reactive flows, *Journal of Computational Physics*, **176**, 247-261.
- [14] Okong'o, N. and Bellan, J., 1994, Consistent boundary conditions for multicomponent real gas mixtures based on characteristic waves, *Journal of Computational Physics*, **176**, 330-344.
- [15] Poinso, T.J. and Veynante, D., 2001, *Theoretical and Numerical Combustion*, R.T. Edwards Inc, Philadelphia.
- [16] Sutherland, J.C. and Kennedy, C.A., 2003, Improved boundary conditions for viscous, reacting, compressible flows, *Journal of Computational Physics*, **191**, 502-524.
- [17] Yoo, C.S., Wang, Y., Trouvé, A., and Im, H.G., 2005, Characteristic boundary conditions for direct numerical simulations of turbulent counterflow flames, *Combustion Theory and Modelling*, **9**, 617-646.
- [18] Nicoud, F., 1999, Defining wave amplitude in characteristic boundary conditions, *Journal of Computational Physics*, **148**, 418-422.
- [19] Valorani, M. and Favini, B., 1998, On the numerical integration of multi-dimensional, initial boundary value problems for the Euler equations in Quasi-Linear Form. *Numerical Methods for Partial Differential Equations*, **14**, 781-814.

- [20] Prosser, R. and Schlüter, J., 2004, Toward improved boundary conditions DNS and LES of turbulent subsonic flows. *Proceedings of Summer Program*, Center for Turbulence Research, Stanford University, 395-410.
- [21] Prosser, R., 2005, Improved boundary conditions for the direct numerical simulation of turbulent subsonic flows. I. Inviscid flows, *Journal of Computational Physics*, **207**, 736-768.
- [22] Mueller, M.A., Yetter, R.A., and Dryer, F.L., 1998, Measurement of the rate constant for  $\text{H} + \text{O}_2 + \text{M} \rightarrow \text{HO}_2 + \text{M}$  ( $\text{M} = \text{N}_2, \text{Ar}$ ) using kinetic modeling of the high-pressure  $\text{H}_2/\text{O}_2/\text{NO}_x$  reaction, *Proceedings of Combustion Institute*, **27**, 177-184.
- [23] Müller, B., 1999, Low Mach number asymptotics of the Navier-Stokes equations and numerical implications, *von Karman Institute for Fluid Dynamics Lecture Series 1999-03*, 30<sup>th</sup> computational fluid dynamics.
- [24] Giles, M.B., 1990, Nonreflecting boundary conditions for Euler equation calculations, *AIAA Journal*, **28**, 2050-2058.
- [25] Yoo, C.S. and Im, H.G., 2005, Transient dynamics of edge flames in a laminar nonpremixed hydrogen-air counterflow, *Proceedings of Combustion Institute*, **30**, 349-356.
- [26] Hinze, J.O., 1975, *Turbulence* (2nd ed.), McGraw-Hill, New York.
- [27] Colonius, T., 2004, Modeling artificial boundary conditions for compressible flow. *Annual Review of Fluid Mechanics*, **36**, 315–345.
- [28] Kennedy, C.A., 2002, *Private Communication*.
- [29] Hirsch, C., 1990, *Numerical computation of internal and external flow Vol 2*, Wiley, New York.

- [30] Kee, R.J., Grcar, J.F., Smooke, M.D., and Miller, J.A., 1985, *A Fortran Program for Modeling Steady Laminar One-Dimensional Premixed Flames*, Sandia National Laboratories Report SAND85-8240.

### List of Figures

- Figure 1 Temporal variations of vorticity isocontours for Cases A1–A3. From top to bottom,  $t = 0, 36, 56$ , and  $72 \mu\text{sec}$ .
- Figure 2 Temporal variations of  $y$ -directional velocity isocontours for Cases A1–A3. From top to bottom,  $t = 0, 36, 56$ , and  $72 \mu\text{sec}$ .
- Figure 3 Temporal variations of  $x$ -directional velocity isocontours for Cases A1–A3. From top to bottom,  $t = 0, 36, 56$ , and  $72 \mu\text{sec}$ .
- Figure 4 Temporal variations of pressure isocontours for Cases A1–A3. From top to bottom,  $t = 0, 36, 56$ , and  $72 \mu\text{sec}$ .
- Figure 5 Temporal variation of the L2-norm of pressure difference normalized by the initial value for Cases A1–A3.
- Figure 6 Temporal variation of the L2-norm of pressure difference normalized by the initial value for the improved boundary condition with  $M = 0.025 \sim 0.150$ .
- Figure 7 Temporal variations of (a) minimum pressure [atm] and (b) L2-norm of pressure difference for Cases B1–B4.
- Figure 8 Temporal variations of temperature for Cases C1–C3. From top to bottom,  $t = 12, 18, 22$ , and  $27 \mu\text{sec}$ .
- Figure 9 Temporal variations of  $Y_{\text{HO}_2}$  isocontours for Cases C1–C3. From top to bottom,  $t = 12, 18, 22$ , and  $27 \mu\text{sec}$ .
- Figure 10 Temporal variations of the maximum and minimum pressure for Cases D1–D3.
- Figure 11 Steady pressure isocontours [atm] for Cases D1–D3.
- Figure 12 Steady  $v$  isocontours [cm/s] for Cases D1–D3.

Figure 13 Temperature, pressure,  $u$  and  $v$  isocontours of H<sub>2</sub>-air premixed flame in a 2-D channel at  $t = 1.0$  msec.

Figure 14 Temporal variations of (a) the minimum pressure and (b) the L2-norm of the pressure difference for Cases E1-E3.

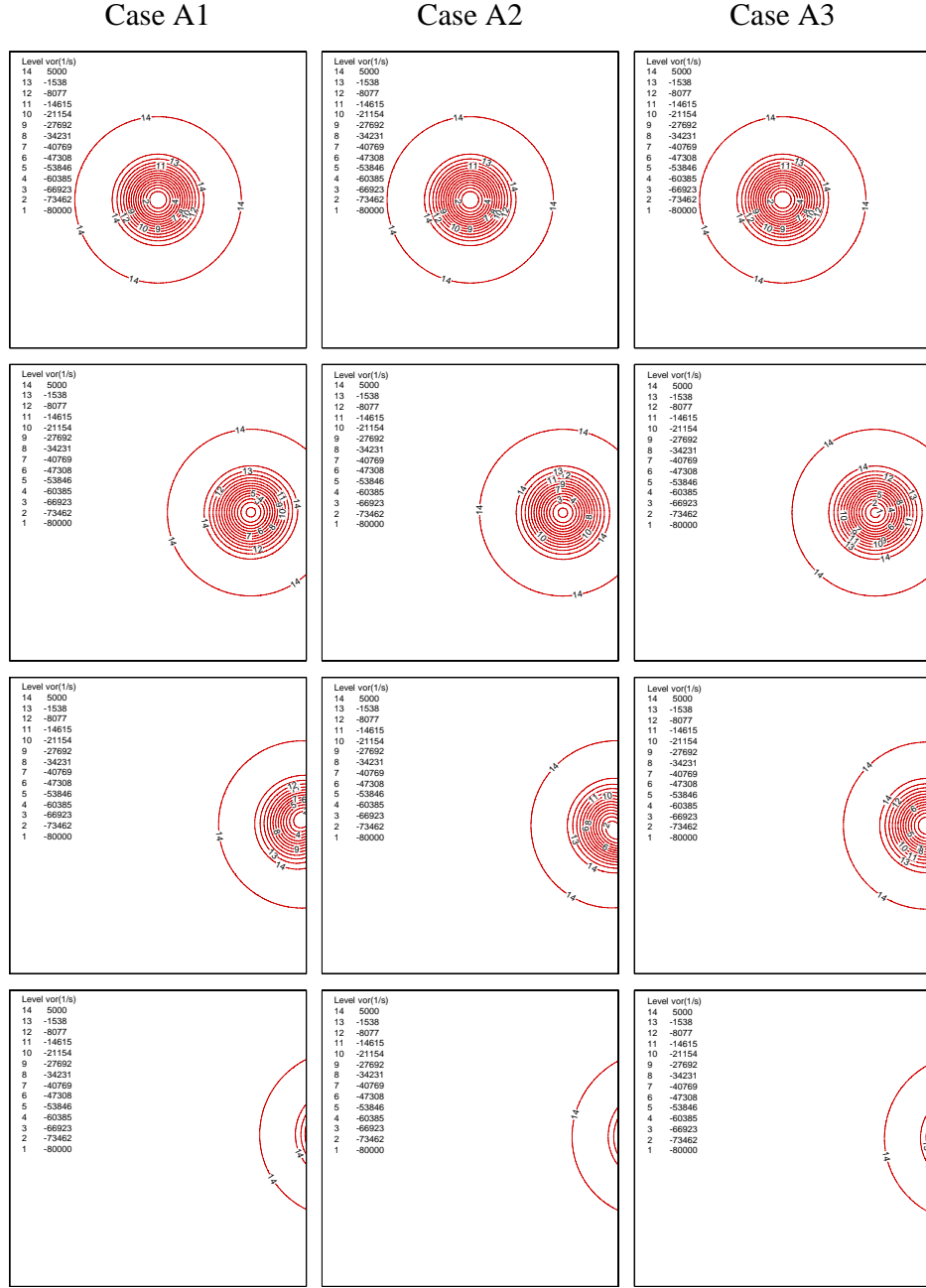


Figure 1 Temporal variations of vorticity isocontours for Cases A1–A3. From top to bottom,  $t = 0, 36, 56$ , and  $72 \mu\text{sec}$ .



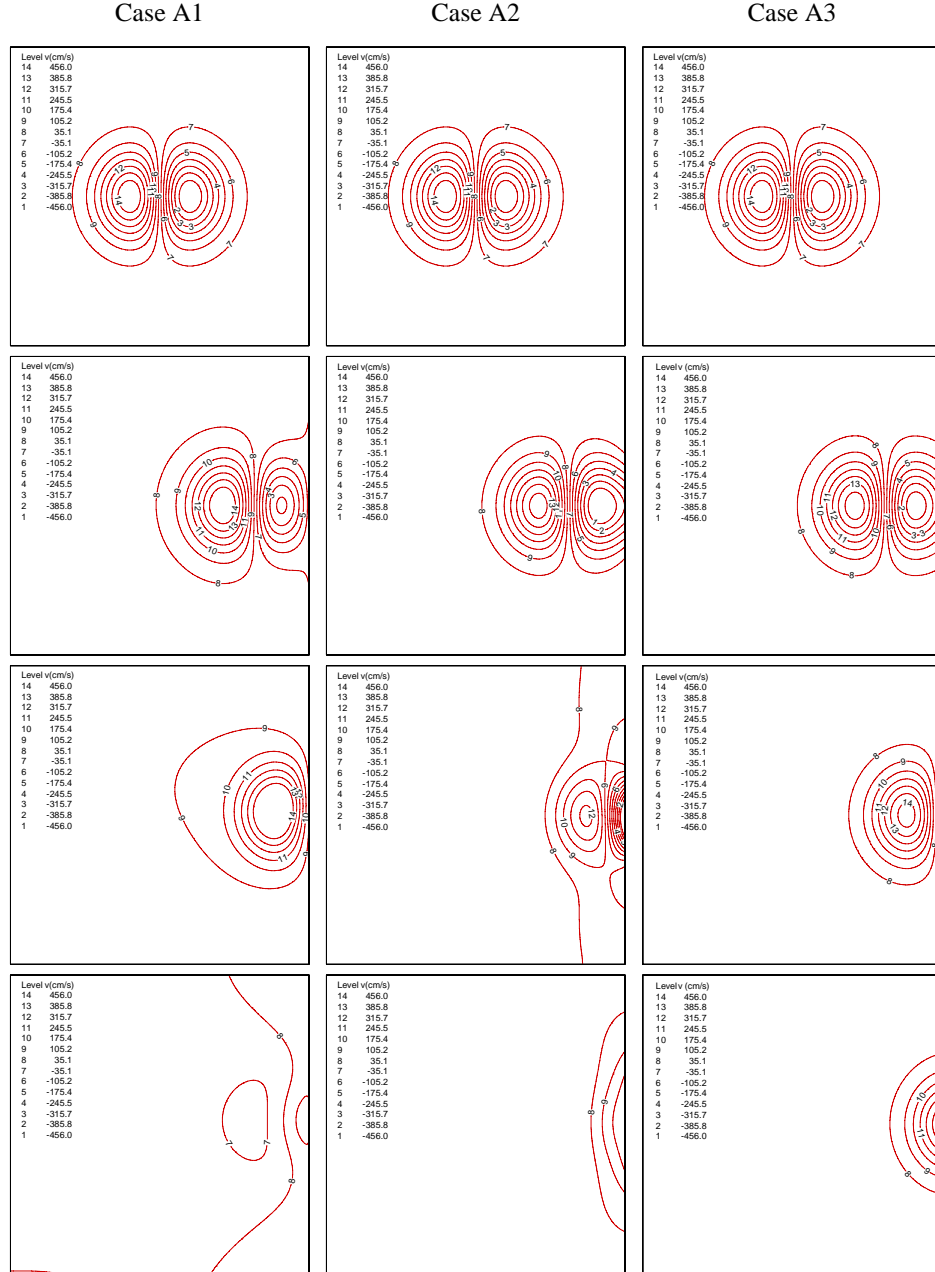


Figure 2 Temporal variations of y-directional velocity isocontours for Cases A1–A3. From top to bottom,  $t = 0, 36, 56$ , and  $72 \mu\text{sec}$ .

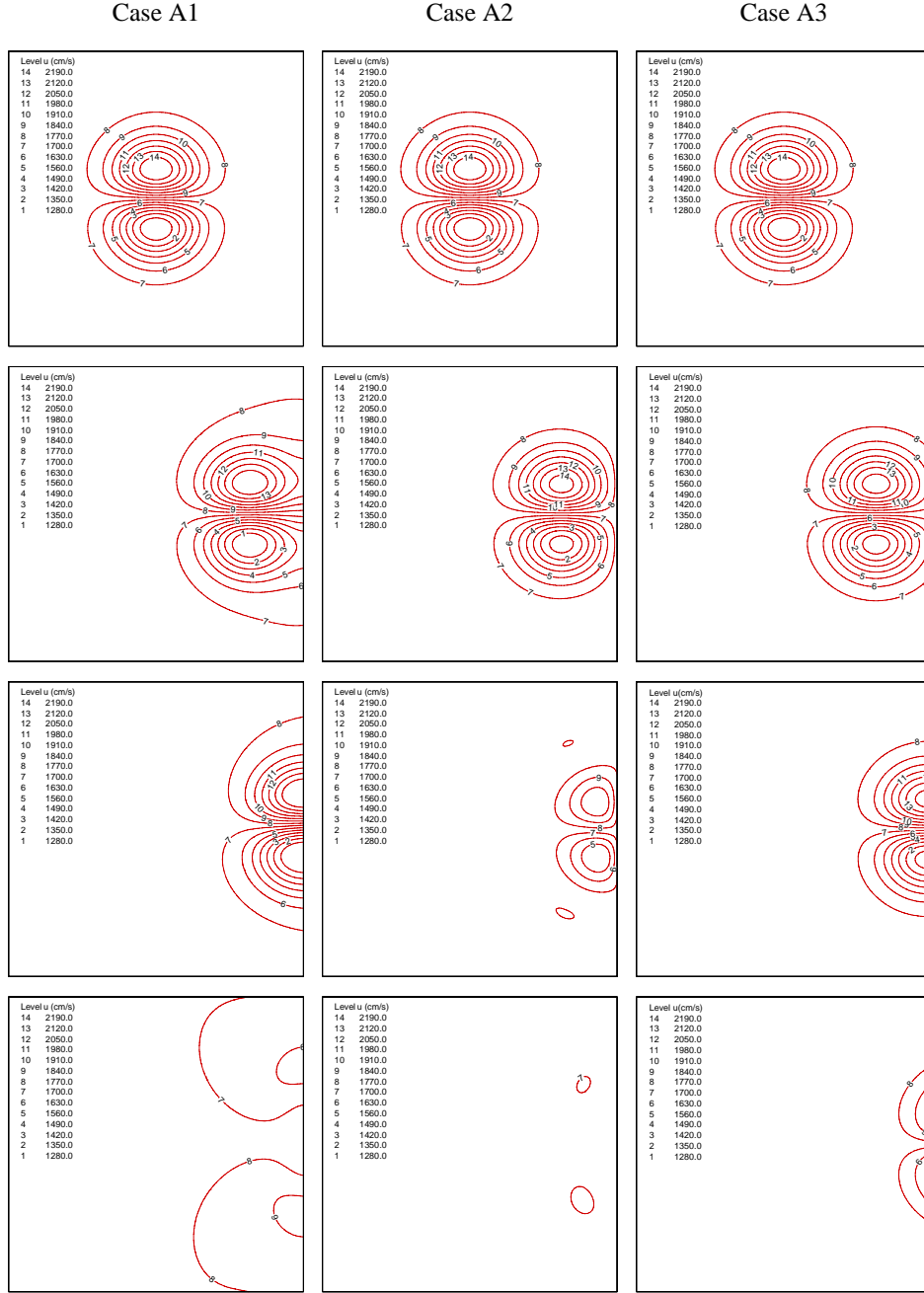


Figure 3 Temporal variations of  $x$ -directional velocity isocontours for Cases A1–A3. From top to bottom,  $t = 0, 36, 56$ , and  $72 \mu\text{sec}$ .

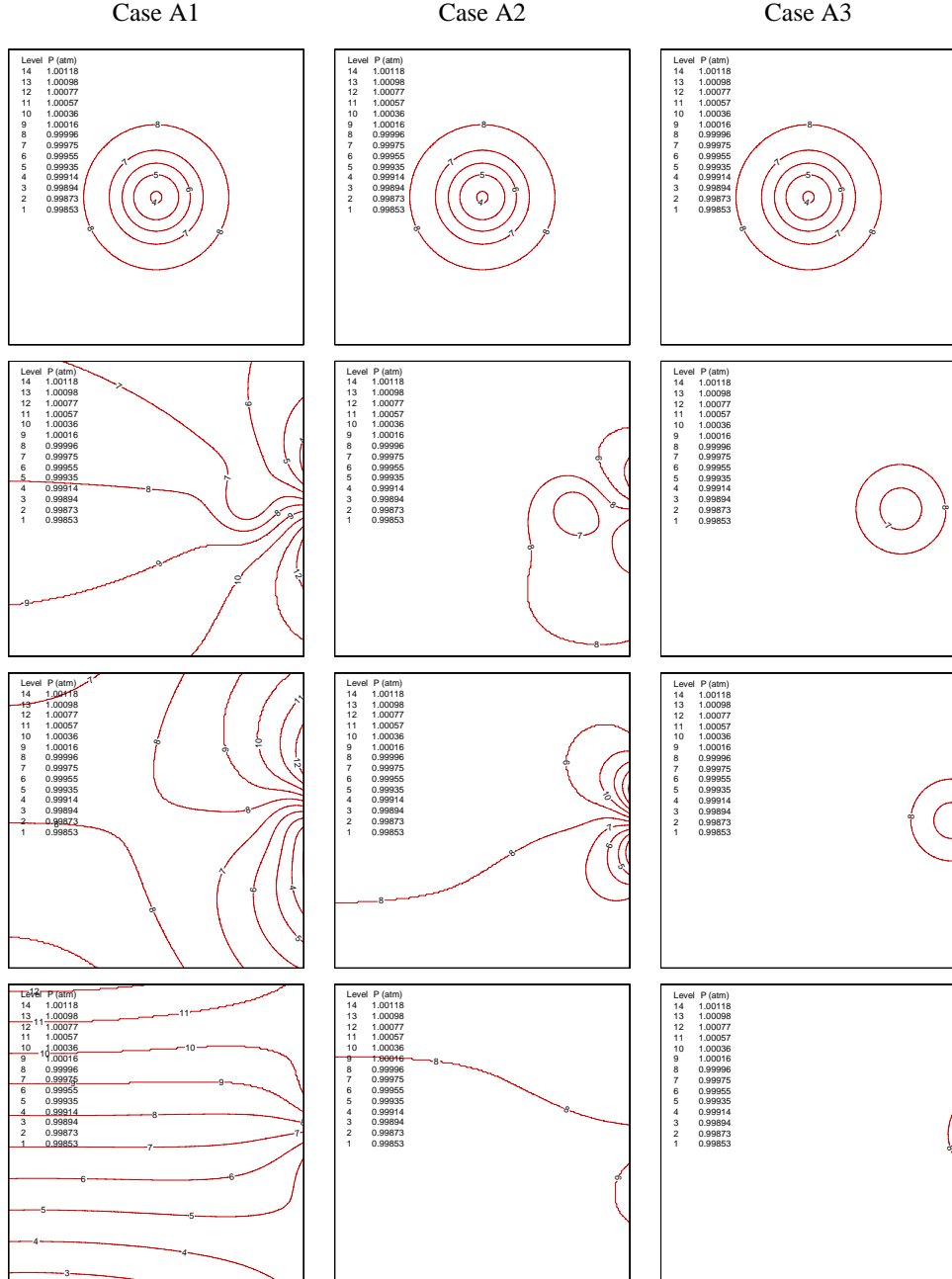


Figure 4 Temporal variations of pressure isocontours for Cases A1–A3. From top to bottom,  $t = 0, 36, 56, \text{ and } 72 \mu\text{sec}$ .

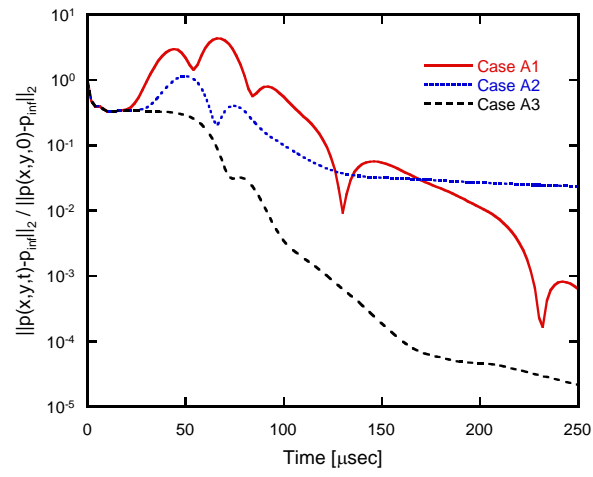


Figure 5 Temporal variation of the L2-norm of pressure difference normalized by the initial value for Cases A1–A3.

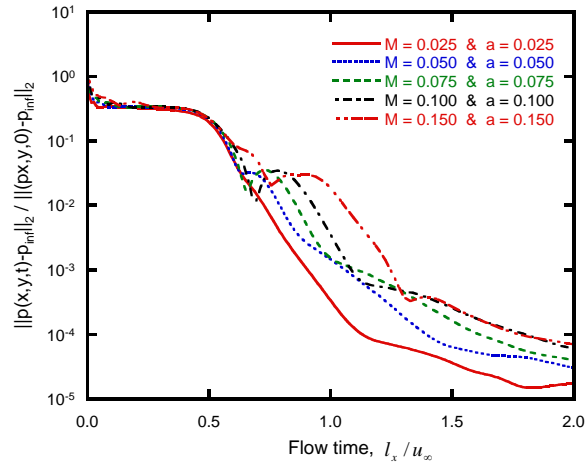
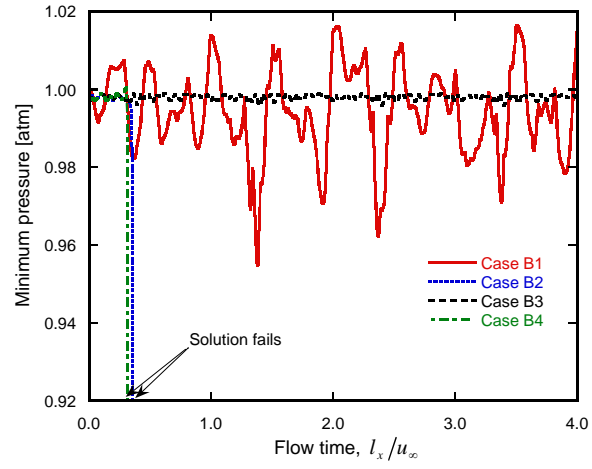
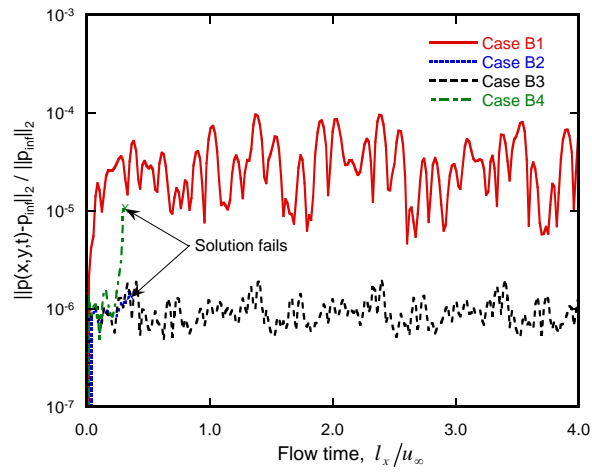


Figure 6 Temporal variation of the L2-norm of pressure difference normalized by the initial value for the improved boundary condition at various Mach numbers.



(a) Minimum pressure [atm]



(b) L2-norm of pressure difference

Figure 7 Temporal variations of (a) minimum pressure [atm] and (b) L2-norm of pressure difference for Cases B1–B4.

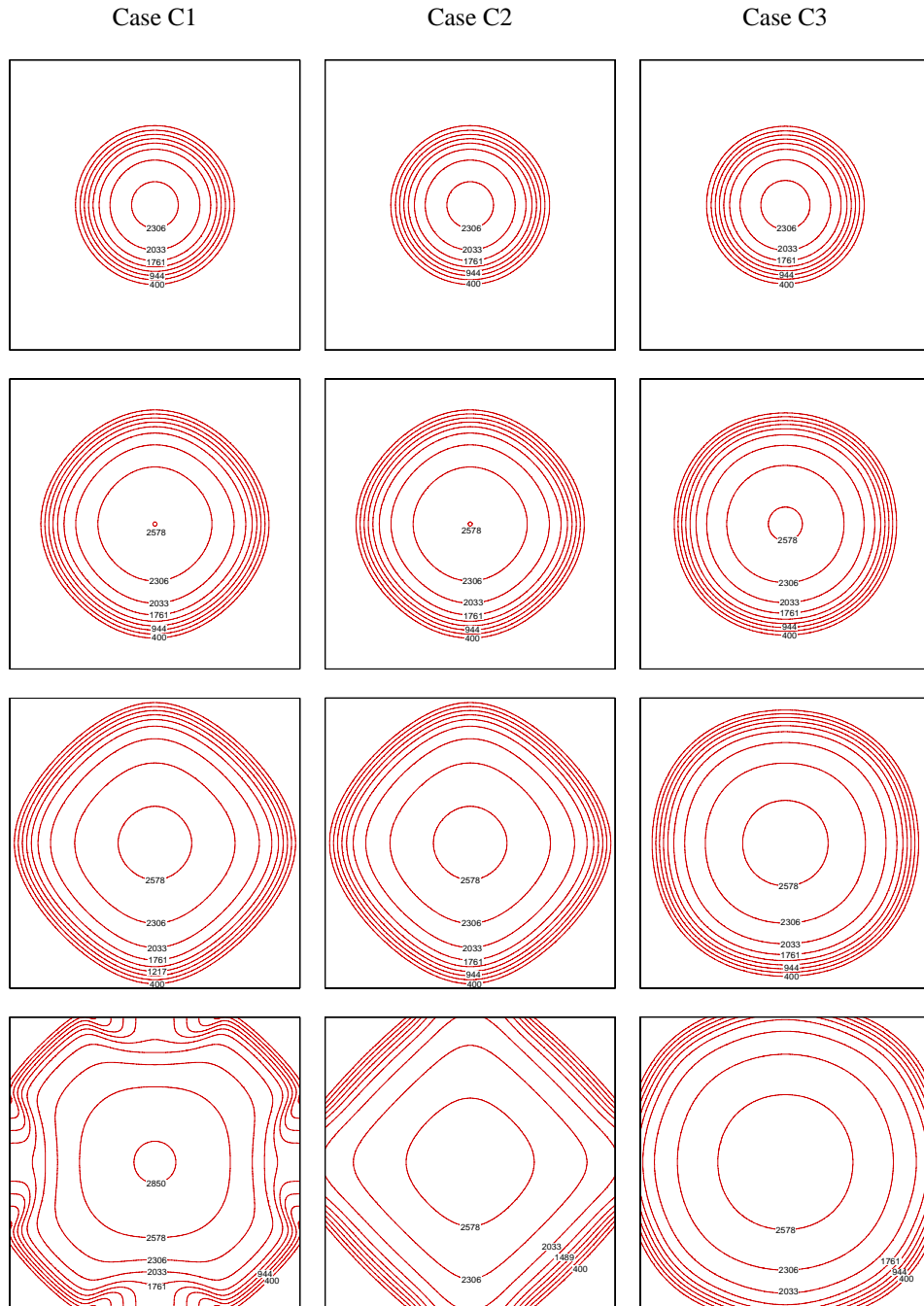


Figure 8 Temporal variations of temperature for Cases C1-C3. From top to bottom,  $t = 12, 18, 22,$  and  $27 \mu\text{sec}$ .

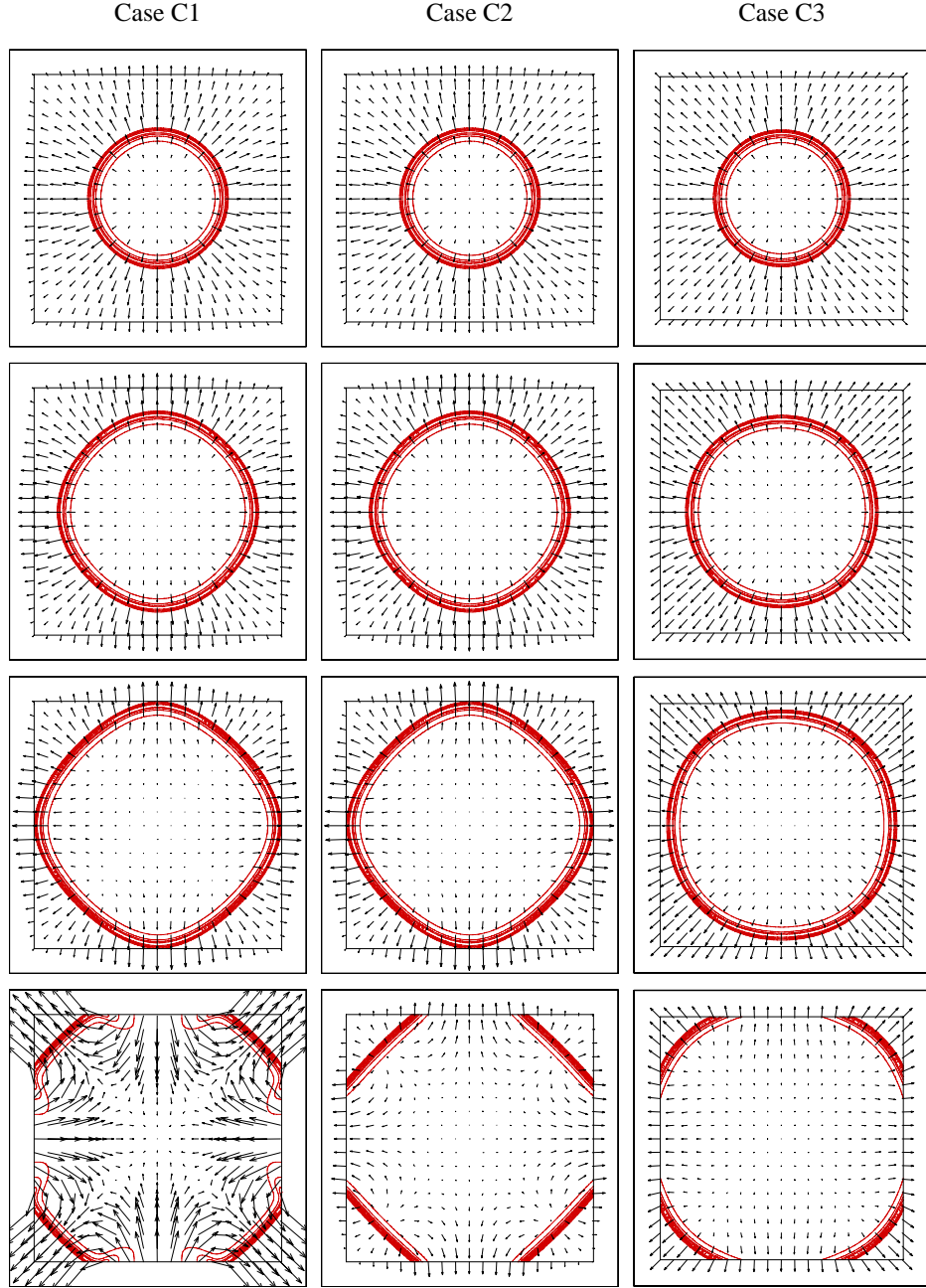


Figure 9 Temporal variations of  $Y_{\text{HO}_2}$  isocontours (lines) and the velocity field (vectors) for Cases C1-C3. From top to bottom,  $t = 12, 18, 22,$  and  $27 \mu\text{sec}$ .



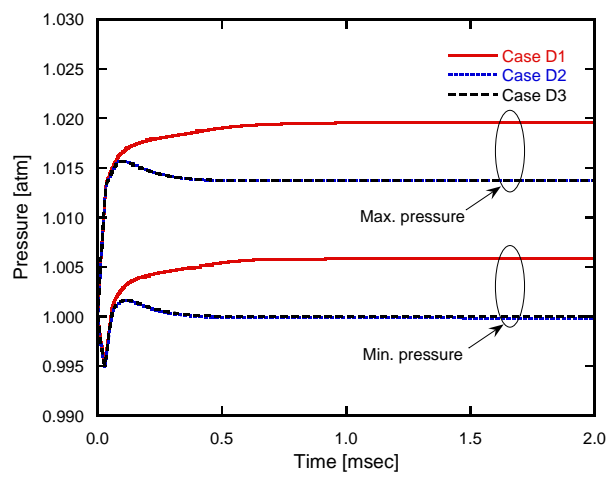


Figure 10 Temporal variations of the maximum and minimum pressure for Cases D1–D3.

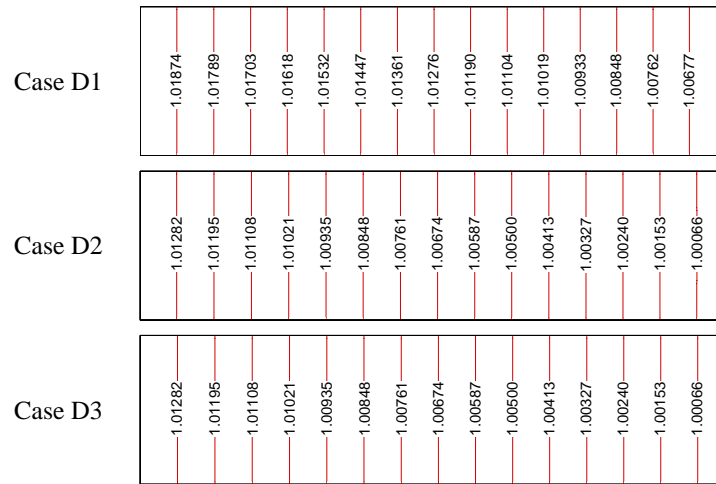


Figure 11 Steady pressure isocontours [atm] for Cases D1–D3.

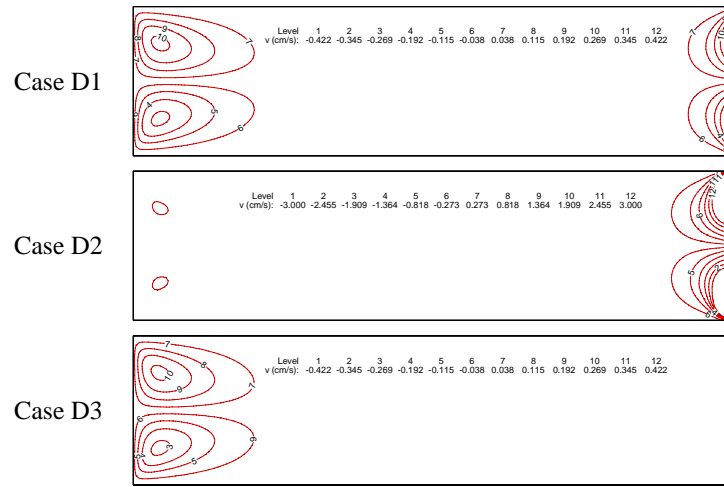


Figure 12 Steady  $v$  isocontours [cm/s] for Cases D1–D3.

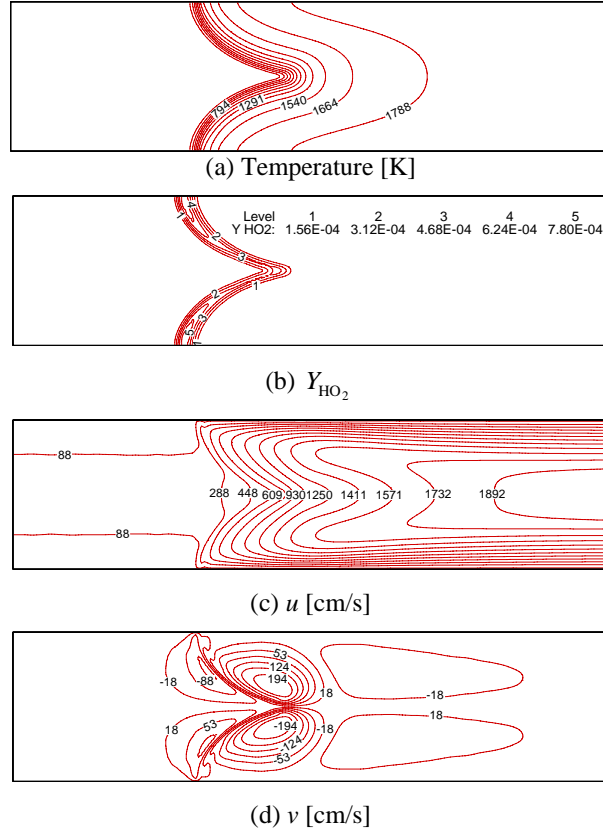
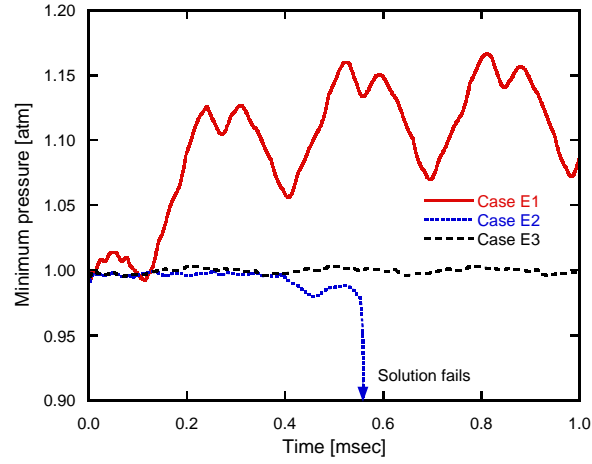
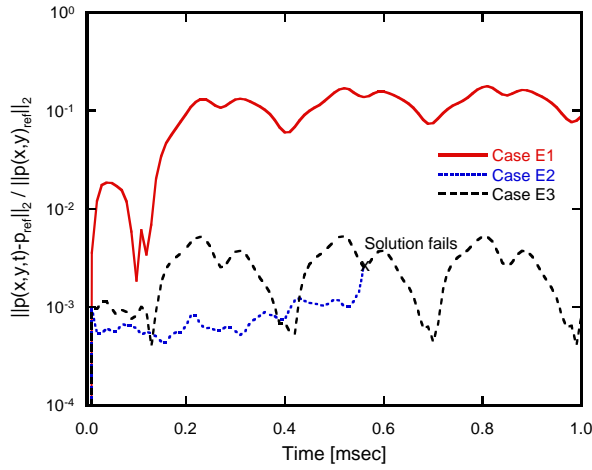


Figure 13 Temperature, pressure,  $u$  and  $v$  isocontours of  $\text{H}_2$ -air premixed flame in a 2-D channel at  $t = 1.0$  msec.



(a) Minimum pressure [atm]



(b) L2-norm of pressure difference

Figure 14 Temporal variations of (a) the minimum pressure and (b) the L2-norm of the pressure difference for Cases E1–E3.